Chapter 7

Experimental Investigation of the Influence of Combustor Cooling on the Characteristics of a FLOX©-Based Micro Gas Turbine Combustor

Jan Zanger, Monz Thomas and Aigner Manfred

Additional information is available at the end of the chapter

http://dx.doi.org/10.5772/54405

1. Introduction

Decentralised combined heat and power generation (CHP) offers a higly efficient and sustainable way for domestic and industrial energy supply. In contrast to electrical power generation by large scale power plants in the MW-range the waste heat of the electical power generation of Micro-CHP-Units can be used by the customer without extensive grid losses. Using the combined heat and power concept overall power plant efficiencies of up to 90 % for sub MW-range CHP-units are possible [1]. In recent CHP plants conventional piston gas engines are mostly used since these systems show a good electric efficiency paired with moderate investment costs. On the other hand cycles based on micro gas turbine (MGT) systems have the potential to play an important role in decentralised power generation. In small plants for distributed power generation the flexible application of different gaseous fuels (natural gas qualities, bio fuels and low calorific gases) is an important factor. Furthermore, the national standards for exhaust gas emission levels need to be met not only at the time of installation but also after years of operation. Here, compared to piston engines MGT systems have advantages regarding fuel flexibility, maintenance costs and exhaust gas emissions [2]. This gives the possibility to avoid the installation of a cost-intensive exhaust gas treatment. Due to higher exhaust gas temperatures MGTs are more suitable for the generation of process heat and cooling. Furthermore, MGTs can be operated in a wider range of fuel gas calorific value and they are less sensitive to the fuel gas composition. Beside the advantages MGT systems need to be optimised in terms of electric efficiency which is recently at $\approx$ 30% in natural gas operation.

In order to increase fuel flexibility, electrical efficiency, product life time and reliability of micro gas turbine systems while meeting today's and future exhaust gas emission levels, further development of the combustion systems needs to be done. To meet these tasks innovative combustion concepts are needed.

Modern combustion systems for MGTs are mainly based on swirl-stabilised lean premixed concepts which promise low levels of exhaust gas pollutants. Here, the central recirculation

zone induced by the swirl of the income air flow serves to stabilise the flame of the main stage generating compact flames. However, these combustion systems tend to a liability to thermo-acoustic instabilities and coherent flow structures like PVC, especially at lean premixed conditions [3, 4] which can cause high amplitude pressure oscillations. This can lead to serious damage of components in the combustion system as well as the turbo engine itself. In addition, oscillating pressure and heat release zones as well as local flame extinction, caused by coherent flow structures can have a huge impact on the production of combustion emissions. Moreover, swirl-stabilised combustion is limited in using different fuel gas compositions regarding flame flashback incidences [5] and reliable operation range. In particular, fuel gas compositions with high hydrogen fractions limit the application of swirl-stabilised combustion concepts. Studies have shown the potential of the Flameless Oxidation (FLOX©)[6] based jet-stabilised combustion concept to achieve both low exhaust gas emission levels and reduced risk towards thermo-acoustic instabilities in combination with high fuel flexibility. As discussed by Hambdi et al. [7] the general idea of this concept is also known as MILD combustion [8], colourless distributed combustion [9] or high temperature air combustion (HiTAC) [10] to name a few. The main characteristic which all those similar concepts share is the use of high temperature process air and a high dilution of the fresh gas mixture by recirculated flue gases. In particular the FLOX©-concept is characterised by non-swirled technically premixed high impulse jets penetrating a combustion chamber in a circular arrangement. These jets drive a strong inner recirculation resulting in an effective mixing process of hot exhaust gases and the fresh incoming fuel/air mixture. This enhances the flame stabilisation but also reduces the chemical reaction rates by a strong dilution. Hence, the reaction zone is stretched over a larger volume compared to swirl-stabilised combustion concepts. This volumetric reaction region exhibits an almost homogeneously distributed temperature profile inside the combustion chamber close to the adiabatic flame temperature of the global equivalence ratio Φ promising low NOx emission levels [11]. Due to the high momentum jets and therefore, the absence of low velocity zones of the income air mixture, the combustion concept has a high resistance to flashback incidents even at highly premixed conditions [12] and high hydrogen fractions [13].

Typical temperature and velocity fields of a FLOX©-based combustor are exemplarily reported by Schütz et al. [14]. Combustion stability, limits of the flameless regime as well as a comparison between experimental and numerical results obtained by Large-Eddy Simulation is reported by Duwig et al. [15]. Lückerath et al. [12] compared OH-PLIF and OH*-chemiluminescence images of a jet-stabilised burner for thermal powers up to 475kW at elevated pressure. Major species concentrations, velocity and temperature fields as well as reaction regions were reported by Lammel et al. [16] for a generic single nozzle setup using particle image velocimetry, laser raman spectroscopy as well as OH-PLIF measurements.

Beside the discussed advantages the implementation of a FLOX©-based combustion concept to a MGT system poses some challenges and tasks. First of all, the quality of the air/fuel premixture has a significant influence on the flame characteristics and emission levels. Therefore, the combustor has to be carefully designed to generate an optimised air/fuel exit profile. Moreover, since MGT systems need to have competitive prices compared to piston engines, the turbo components usually exhibit a most simple design. Therefore, the turbine blades are not cooled internally resulting in much lower turbine inlet temperature limits compared to industrial gas turbines. In order to adjust the turbine inlet temperature profile a

http://dx.doi.org/10.5772/54405

considerable amount of cool compressor air bypasses the combustion chamber and remixes with the hot exhaust gases at the combustion chamber exit. Since the FLOX© combustion at high air numbers exhibits volumetric reaction regions, the combustion requires more room compared to swirl-stabilised combustion concepts. The low production of harmful emissions as well as the high flame stability of the FLOX©-regime would be negatively influenced by the injection of cold dilution air into extensively expanded volumetric reaction zones. Therefore, combustion system design parameters like length of the combustion chamber and position, shape and pattern of dilution holes have to be considered for a final combustor development.

In order to improve flame stability, lifetime, operating range and exhaust gas emissions of the combustion system in a commercial Turbec T100 MGT, a FLOX©-based jet-stabilised combustor was designed for natural gas utilising the advantages of this concept. The recent work covers an experimental study of two combustor configurations differing in the combustor front plate cooling. The paper presents the influence of the combustor cooling air on flame characteristics, lean blow off (LBO) limits and exhaust gas emissions. Flame characteristics are analysed, using measurements of the OH^*-chemiluminescence (OH^*-CL) signal at selected power loads and air numbers. From these images the height above burner, the dispersion of OH^*-CL signal and its homogeneity are derived. These quantaties are discussed with respect to the effects of cooling air, thermal power load and air number on the combustor performance.

2. Experimental setup

2.1. Combustor design

In Figure 1 and 2 both FLOX-based combustor configurations are shown which were used in this study. The reference combustor without any combustor front plate cooling is displayed in Figure 1. In order to increase the combustor lifetime an additional impingement front plate cooling is implemented into the second configuration to decrease the temperature at the location of the highest thermal loads. Both combustor designs consist of 20 fuel and air nozzles in a circular arrangement. Natural gas is injected concentrically into the air nozzles, which are oriented co-axially with respect to the combustion chamber. Both air and fuel gas flow are injected without any swirl. Partial premixing of fuel and air is achieved by the special design of the injecting system. Vortical structures generated by the air injection system provide a macroscopic mixing of fuel and air. Turbulence produced by the fuel injection system provides mixing on a microscopic scale. For the impingement cooling system a small part of the overall air mass flow is fed into a cooling air plenum and passes a perforated plate. This perforated plate produces small cooling air jets impinging the combustor front plate from the back side. After the cooling air has hit the combustor front plate it is led radially through channels and injected into the combustion chamber through 20 holes. The cooling air holes are positioned in between the FLOX© combustor air nozzles on a slightly larger diameter. In addition to the impingement cooling the front plate of the cooled design is coated with a zirconium oxide thermal protection layer.

2.2. Test rig description

In order to run parametric studies of the combustion performance independent from the MGT load point limitations, the combustor was implemented into an atmospheric test rig.

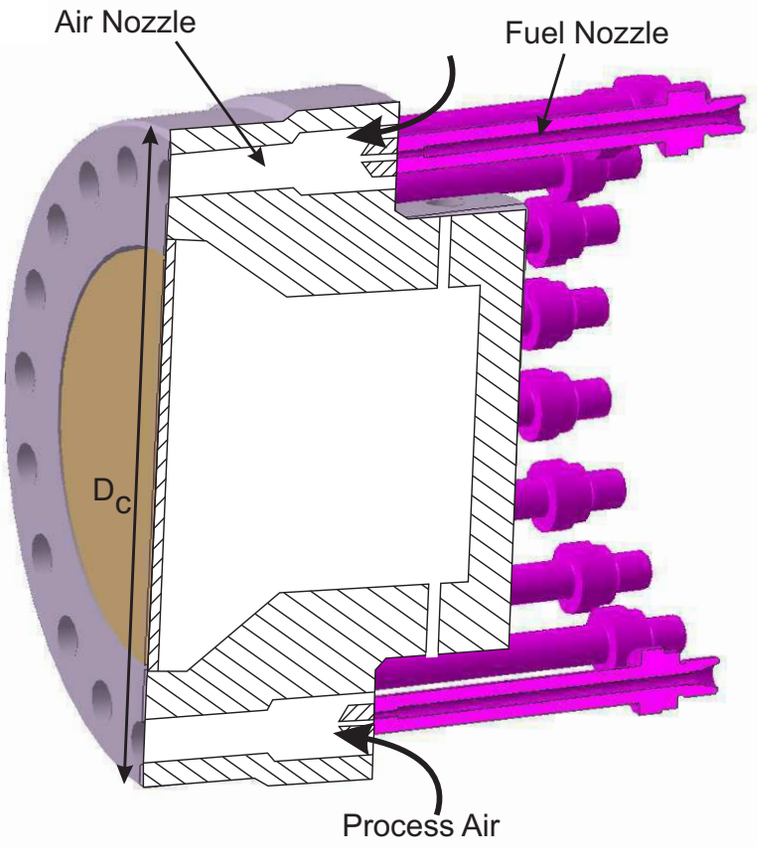

Figure 1. Uncooled Combustor.

The experimental setup shown in Figure 3 comprises the air and fuel supply, the combustor and an optically accessible, hexagonal combustion chamber comprising six quartz glass windows. The hexagonal cross-section was chosen as a trade-off between good optical accessibility and the analogy to the circular cross-section of the original MGT liner. A circular fuel plenum which is situated under the air plenum but not shown in Figure 3 ensures an equal supply of all 20 fuel gas nozzles. In order to emulate the combustor inlet conditions of the MGT the air can be preheated electrically up to 925K by five 15kW "Leister" air heater units. The complete air supply system is decoupled acoustically from the test bench by a perforated plate located at the air inlet. When entering the air plenum the air flow is directed via a baffle in a way that a 180°deflection at the combustor inlet of the original MGT is reproduced. This was found to be essential to generate a specific premixing profile in the combustor nozzle and hence is important for flame characteristics and flame stabilisation. After passing the baffle a small part of the air flow enters the cooling plenum and the major part is fed into the air nozzles of the combustor, where the premixing with the fuel takes place. In this study the combustor is operated with natural gas (LHV = 47.01 $\frac{MJ}{kg}$, AFR_{stoech} = 16.2). On the top of the combustion chamber an exhaust gas duct is flanged.

http://dx.doi.org/10.5772/54405

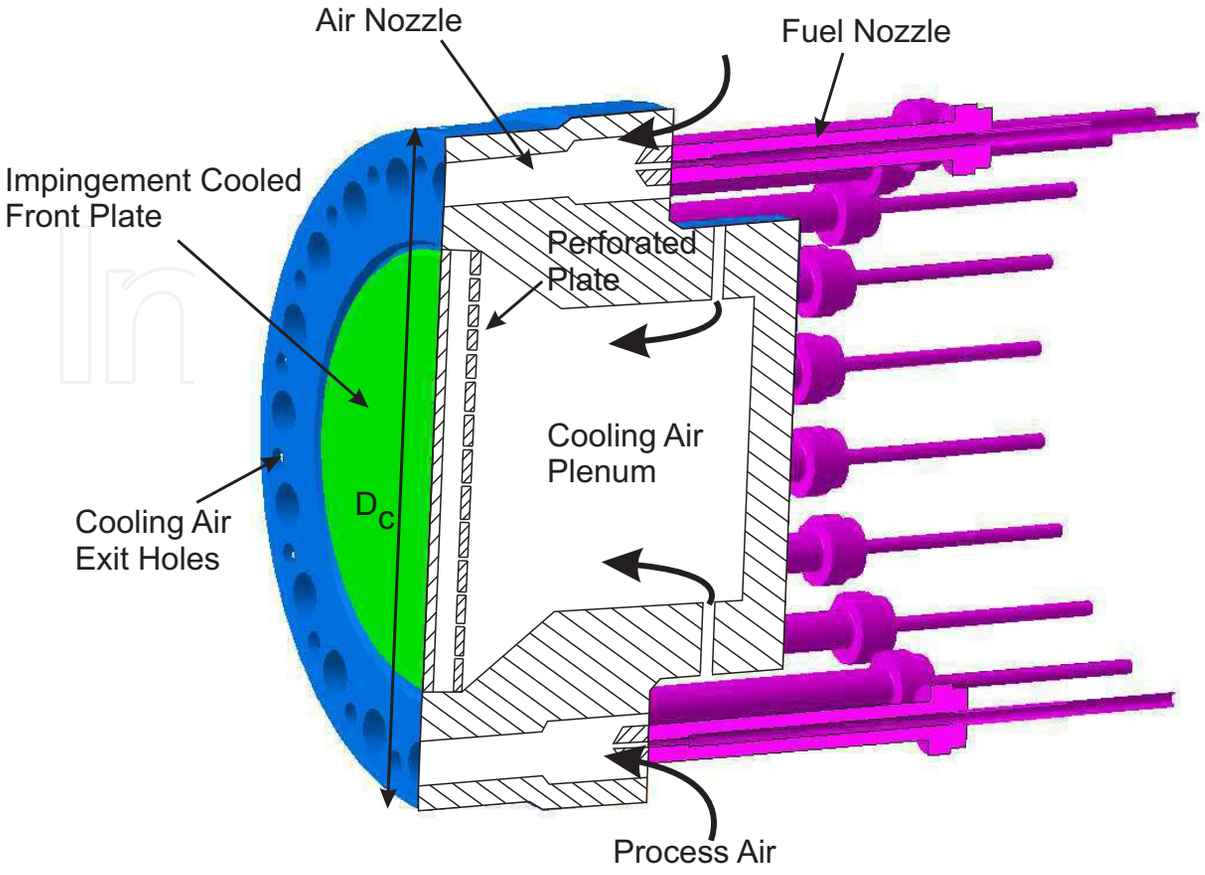

Figure 2. Impingement Cooled Combustor.

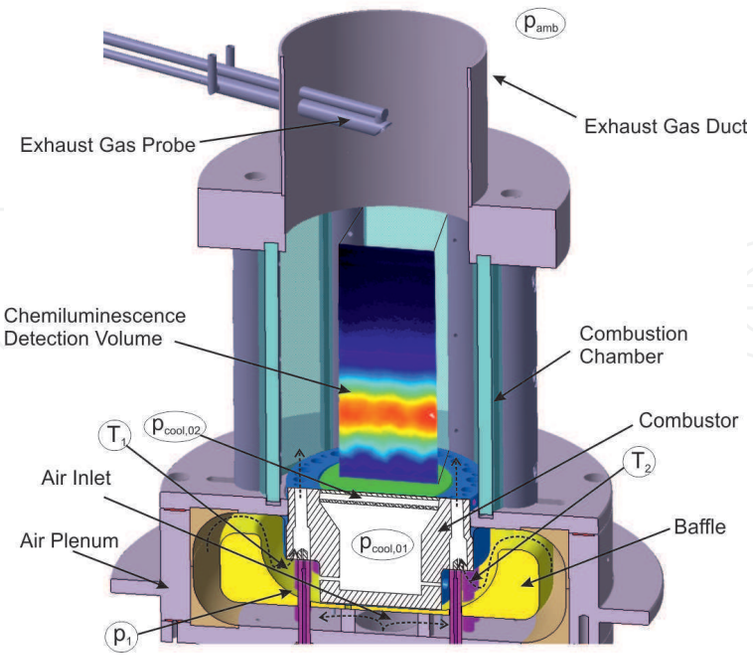

Figure 3. Atmospheric Combustor Test Rig

2.3. Instrumentation

To analyse all relevant process parameters inside the system the test rig is equipped with a detailed instrumentation. The data acquisition at a frequency of 2 Hz is realised by "Delphin" modules. For temperature measurements a total number of 27 thermocouples (type N, precision class 2) are installed. The arithmetic average of the temperature T_1 and T_2 which are situated in the air flow at the combustor inlet defines the combustor preheat temperature T_V with an uncertainty of $\pm 0.85\%$ of the actual value. The rig furthermore comprises 2 total and 13 static pressure transducers read out by pressure scanners "Netscanner Model 9116" and "Model 9032" by Esterline Pressure Systems. All pressures can be optained with a manufacturer's accuracy of ± 4 mbar. Combustor pressure loss is determined by the static pressure p_1 measured short before the combustor inlet (see figure 3) and the ambient pressure. Applying a suitable calibration, the mass flow through the cooling system is calculated as a function of the pressure loss between the static pressures $p_{cool,01}$ and $p_{cool,02}$ situated in front of and behind the perforated plate. The fuel mass flow is controlled by a "Bronkhorst Cori-Flow" coriolis mass flow controller with a manufacturer's accuracy of $\pm 0.5\%$ of the actual value and the air mass flow is regulated by a "Bronkhorst EL-Flow" thermal mass flow controller with a manufacturer's accuracy of $\pm 0.8\%$. As indicated in figure 3 a radially traversable suck-up exhaust gas probe is mounted inside the exhaust gas duct. The probe is equipped with a coaxial air cooling keeping the probe tip at a constant temperature of 120°C to achieve a sufficient quenching of the measured exhaust gas. This ensures defined measuring conditions. The sucked-up exhaust gases are directed via heated hoses to an "ABB" exhaust gas analysing system. The flue gas species O_2, CO, CO_2, NO, NO_2 and unburned hydrocarbons (UHC) are measured by a magnetomechanical analyser "Magnos106", a infrared analyser "Uras14", a UV photometer "Limas11 HW" and a flame ionisation detector "MultiFID14". The species O_2, CO and CO_2 are measured in a dry environment, whereas all other species are detected in wet conditions. The measurements of the species shown in this study have manufacturer's accuracies as indicated in Table 1.

	CO [ppm]	NO_x [ppm]	UHC [ppm]	O_2 [Vol-%]
Range 1	0-8	0-24	0-9	0-25
Accuracy 1	0.1	0.5	0.1	0.25
Range 2	8-80	24-238	9-90	
Accuracy 2	1	5	1	

Table 1. Ranges and Corresponding Accuracies of the Measured Exhaust Gas Species.

OH* chemiluminescence measurements were used to study the shape, location and homogeneity of the heat release zone. The electronically excited OH* radical is formed by chemical reactions in the reaction zone, predominately via $CH + O_2 \rightarrow CO + OH^*$ [17]. Since its lifetime is very short, the emitted OH*-CL signal originates only from within the reaction region. Therefore, the OH*-CL signal is a very good marker for the location and dimension of the reaction zone. However, this technique is a line-of-sight method giving only spatially integrated information in the combustion chamber depth. The OH*-CL emissions were imaged using a "LaVision FlameStar 2" intensified CCD camera in combination with a "Halle" 64mm, f/2 UV lens and a UV interference filter ($\lambda = 312 \pm 20$nm). All OH*-CL data was time-averaged over a time series of 200 instantaneous images acquired with a repetition rate of 3.6Hz. Due to the substantial difference of the OH*-CL signal over the complete load point range the gate width was varied between 18 and 600 μs at maximum gain factor.

http://dx.doi.org/10.5772/54405

As indicated in Figure 4 the detection volume covers four air nozzles on each side of the combustor. Due to assembly restrictions the nozzles on opposing sides are arranged with a small misalignment with respect to the line of sight.

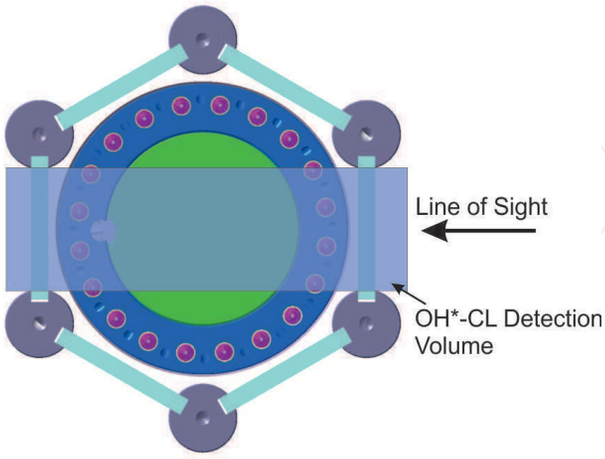

Figure 4. Line of Sight of the OH*-CL measurements

3. Experimental results

The measurements shown in this section were carried out at steady-state combustion conditions, whereupon every single load point is time-averaged over 5 min at an acquisition rate of 2Hz. In order to analyse the operating range of the combustor configurations the overall air number $\lambda_{overall}$ and the thermal power were varied at a constant combustor inlet air preheat temperature T_v. In this study the normalised thermal power $Q_{th,n}$ with respect to MGT full load conditions is presented. The overall air number is defined as the reciprocal of the fuel equivalence ratio Φ calculated with the overall air and fuel mass flows. All mass flows of the MGT load points were scaled to atmospheric conditions keeping the velocity fields constant. Table 2 shows the matrix of the parametric study.

Parameter	Range	Unit
$Q_{th,n}$	35 - 100	%
$\lambda_{overall}$	1.8 - LBO	-
T_v	580	°C

Table 2. Ranges of the Measuring Matrix.

3.1. Operating range

Figure 5 visualises the operating range of the uncooled combustor configuration displaying the normalised axial jet velocity u_{nozzle} at the exit of a single air nozzle as a function of $Q_{th,n}$. U_{nozzle} is defined as

$$u_{nozzle} = \frac{\dot{m}_{nozzle} \cdot R_{mix} \cdot T_{c,in}}{p_{c,in} \cdot A_{nozzle}} / u_{nozzle,max} \quad (1)$$

with the combustor inlet temperature $T_{c,in}$, the static combustor inlet pressure $p_{c,in}$, the planar-averaged specific gas constant of the air/fuel mixture R_{mix}, the nozzle cross-section

area A_{nozzle} and the averaged mass flow of a single nozzle $\dot{m}_{nozzle}$. The whole measuring field of the operating range was scanned by adjusting a constant $Q_{th,n}$ and increasing the $\lambda_{overall}$ up to lean blow-off (LBO) conditions. In this study the lean blow-off is defined as the point where the flame actually extinguishes. The filled points symbolise the feasible operating points whereas the blank points emblematise the points at which LBO occured. All illustrated load points represent an individual measurement which means that no information about the reproducibility of the LBO limit can be given. Regarding the points around LBO it is visible that the feasible $\lambda_{overall}$ slopes with increasing thermal power. The LBO at $Q_{th,n}$ = 35% is with $\lambda_{overall}$ = 3.26 substantially higher compared to $Q_{th,n}$ = 100% with $\lambda_{overall}$ = 3.01. Moreover, figure 5 indicates that higher jet velocities can be realised with increasing $Q_{th,n}$ before LBO occurs. The axial jet velocity u_{nozzle} at LBO significantly varries from 58% at $Q_{th,n}$ = 35% to approximately 140% at $Q_{th,n}$ = 100%. This effect was also observed and discussed by Vaz et al. [18] for a similar system.

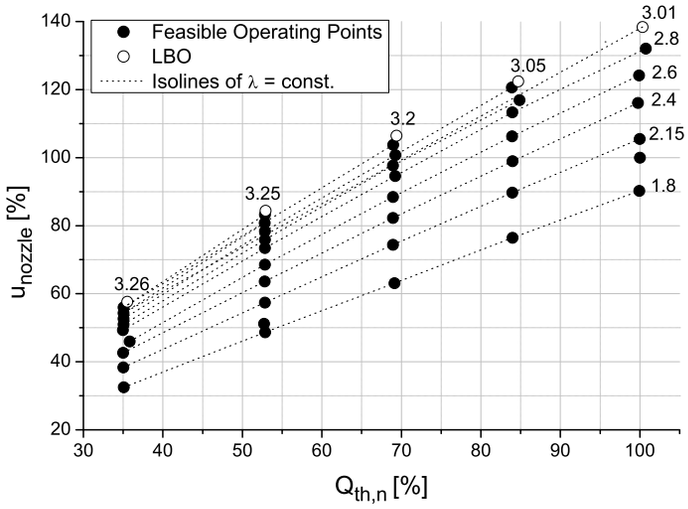

Figure 5. Operating Range of Uncooled Combustor Configuration.

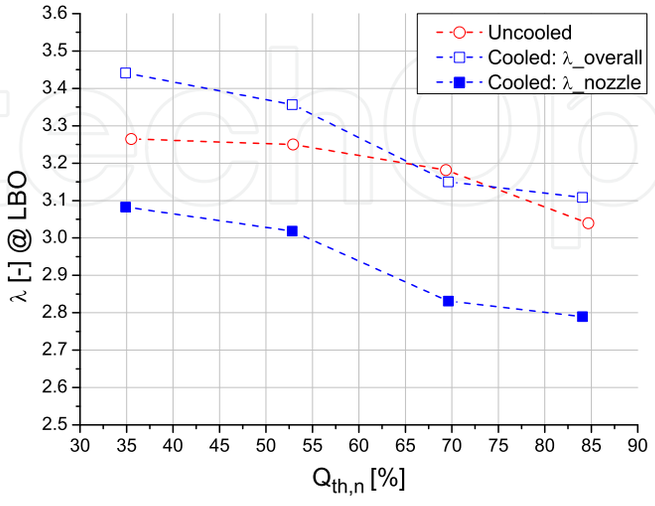

Figure 6. Air Number at LBO of the Cooled and Uncooled Combustor Configurations.

http://dx.doi.org/10.5772/54405

In Figure 6 the comparison between the LBO conditions of the uncooled combustor and the cooled configuration is presented as a function of $Q_{th,n}$. Due to mass flow limitations the LBO of the cooled design could only be measured for $Q_{th}/Q_{th,max} \leq 85\%$, therefore, only this range is visualised. For the cooled design the overall air number $\lambda_{overall}$ of the combustor is shown as well as the local air number λ_{nozzle} of a single nozzle which is reduced by the cooling air mass flow. However, for the uncooled design the local and the overall air numbers are equal due to the lack of cooling air. The $\lambda_{overall}$ at LBO of the cooled configuration follows the general sloping trend of the uncooled design for increasing $Q_{th,n}$ but exhibits a steeper gradient and with $\lambda_{overall}$ = 3.44 at $Q_{th,n}$ = 35% higher values at low thermal loads. This means using a cooled combustor configuration that for $Q_{th}/Q_{th,max} \leq$ 52% more overall air can be fed into the combustion chamber before LBO occurs. This behaviour is advantageous if the amount of combustion air is to be maximised. However, for $Q_{th}/Q_{th,max} \geq 70\%$ the difference between both designs is negligible. Furthermore, the graph of the cooled design exhibits a kink at $Q_{th,n}$ = 70%. This behaviour is reproducible but in order to give a conclusive explanation further investigation need to be carried out. Regarding λ_{nozzle} the cooled configuration exhibits a much lower LBO limit for the whole operating range, whereas the difference between the designs increases with rising thermal power. This indicates that the fraction of cooling air, which interacts with the combustion process, changes with $Q_{th,n}$.

3.2. Exhaust gas emissions

The carbon monoxide (CO) exhaust gas emission profiles of the uncooled combustor configuration are shown in figure 7 as a function of $\lambda_{overall}$ for all thermal powers, whereas CO is normalised to 15% oxygen concentration. All curves exhibit a similar U-shape with a distinct minimum. Regarding the graph at $Q_{th,n}$ = 100% the CO concentrations decrease from 50 ppm at $\lambda_{overall}$ = 1.8 to 24 ppm at $\lambda_{overall}$ = 2.42 followed by a rise up to 58 ppm at $\lambda_{overall}$ = 2.8. In the left hand branch of the CO curves the trend of the measured concentrations follow the trend of the equilibrium conditions which decrease for higher air numbers [19]. The right hand branch, however, is dominated by non-equilibrium effects [20]. Here, the residence time of the flue gases inside the combustion chamber before reaching the exhaust gas probe is insufficiently long to achieve equilibrium state resulting in higher measured CO concentrations. Moreover, due to the expansion of the reaction zones at LBO-near overall air numbers, decribed in section 3.3, the exhaust gas probe is for these conditions located inside the reaction zone resulting in incomplete combustion process at the position of measurement. Regarding the CO profiles at different thermal powers a destinct layered arrangement is observable showing higher CO concentrations for increasing $Q_{th,n}$. Here again, the influence of the residence time is visible since at constant $\lambda_{overall}$ higher thermal powers exhibit higher fuel and air mass flows reducing the overall residence time.

In figure 8 the comparison between the CO profiles of the uncooled combustor and the cooled configuration is shown as a function of λ_{nozzle}. For clarity reasons only the profiles for $Q_{th,n}$ = 53% and 100% are visualised exemplarily but it should be mentioned that the trend of the displayed curves applies to the other thermal powers as well. The CO profiles of both combustor designs show similar U-shaped trends. But it is clearly visible that the profiles of the cooled configuration are shifted horizontally to lower air numbers. The magnitude of the shift is thereby dependent on thermal power. For $Q_{th,n}$ = 100% the shift seems to be approximately constant for all λ_{nozzle}, however, for $Q_{th,n}$ = 53% the CO profiles fit well at

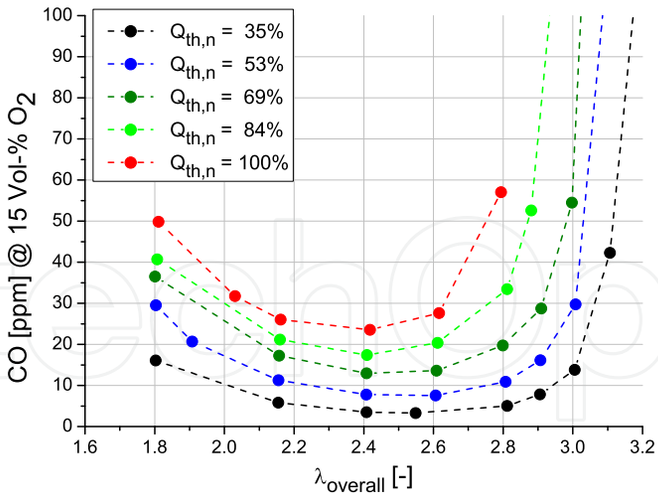

Figure 7. CO Emissions of the Uncooled Combustor Configuration.

low air numbers but differ at high λ_{nozzle}. Due to a high sensitivity to the cooling air mass flow's error the maximum uncertainty of λ_{nozzle} after propagation of error is approximately $\pm 5\%$ for the cooled configuration. However, the uncooled design exhibits an uncertainty better than 1% due to the lack of cooling air. Nevertheless, since the observed shift of the CO profiles shows a distinct systematic trend, it is believed to represent a physical effect.
When comparing the CO emissions of both combustor designs with respect to $\lambda_{overall}$, see figure 9, the difference between both configurations is even more pronounced but shifted to the opposite direction compared to the display as a function of λ_{nozzle}. In the case that the CO profiles of the cooled configuration were equal to the uncooled design for $\lambda_{overall}$ this would suggest that all cooling air participates in the reaction process. On the other hand equal CO profiles for λ_{nozzle} would mean that no cooling air enters the reaction region. Therefore, the observed behaviour indicates that only a part of the cooling air participates in the primary reaction zone.

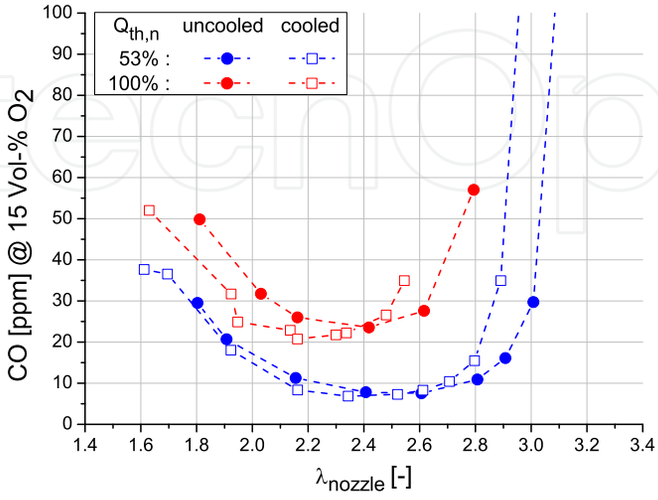

Figure 8. CO Emissions of the Cooled and Uncooled Combustor Designs as a Function of λ_{nozzle}.

http://dx.doi.org/10.5772/54405

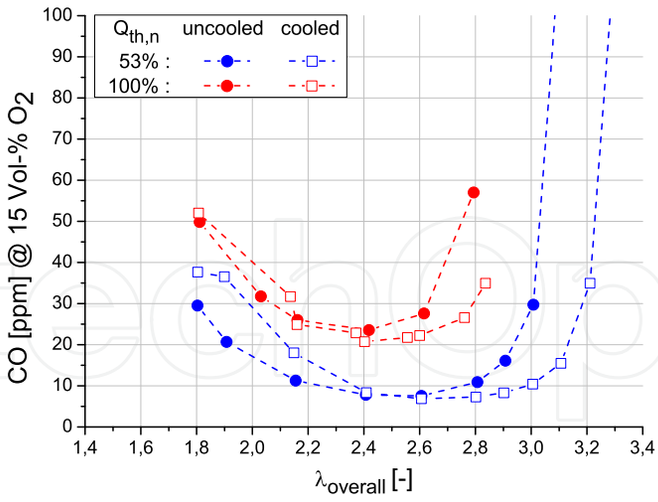

Figure 9. CO Emissions of the Cooled and Uncooled Combustor Designs as a Function of $\lambda_{overall}$.

In order to approximate the amount of cooling air which interacts with the reaction region, the λ_{nozzle} of the cooled configuration is modified in a way that the CO profiles of both combustor designs fit well as shown in figure 10. This new air number is called λ_{nozzle}(mod). For the cooled design it is approximately $\lambda_{nozzle}(\text{mod}) \approx \lambda_{nozzle} + 0.1 \neq const.$ and for the uncooled configuration it equals λ_{nozzle}. This modified air number, which is based on the CO emissions, is an auxiliary quantity for comparing both combustor configurations. Since the visualisation as a function of λ_{nozzle}(mod) neutralises the shift of air number between both designs, the comparison of the magnitudes of certain quantities are facilitated. Therefore, the modified air number is used in the following sections to characterise the difference of both combustor designs.

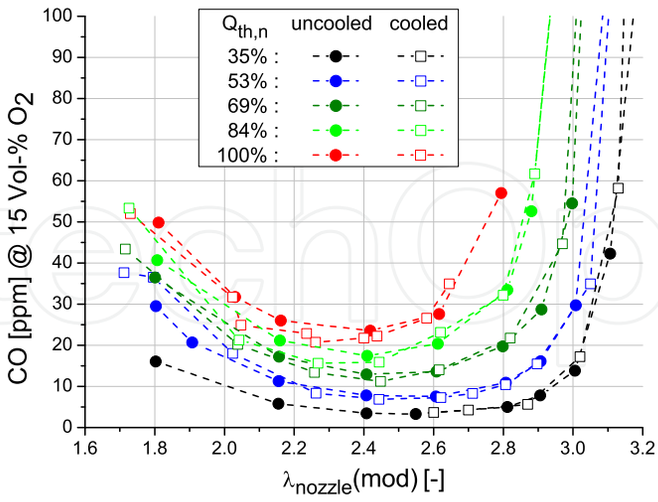

Figure 10. CO Emissions of the Cooled and Uncooled Combustor Configurations as a Function of the Modified Air Number λ_{nozzle}(mod).

The nitrogen oxide (NOx) emissions at 15% O_2 of both combustor designs are visualised in figure 11 as a function of λ_{nozzle}(mod) for $Q_{th,n}$ = 53% and 100%. All NOx profiles show a similar exponential decreasing characteristics and similar magnitudes for rising modified

nozzle air numbers. For $Q_{th,n}$ = 100% the NOx emissions reduce from 18ppm at λ_{nozzle}(mod) = 1.75 down to 2 ppm at λ_{nozzle}(mod) = 2.8 for both combustors. Since the measurements were conducted at lean atmospheric conditions using natural gas, the major NOx formation mechanism is the thermal dominated Zeldovich mechanism. Therefore, the trend of the NOx profiles reflects the exponential decrease of the thermal NOx formation with falling flame temperature and rising air number, respectively. With respect to the profiles at different thermal powers, a very low dependence on $Q_{th,n}$ can be observed. For the uncooled design the curves of all thermal powers match very well, however, for the cooled configuration the NOx profiles at $Q_{th,n}$< 100% exhibit slightly higher magnitudes at low λ_{nozzle}(mod) compared to full load conditions. Regarding the fact that the NOx emissions of both combustor designs fit very well as a function of λ_{nozzle}(mod), the significance of this modified nozzle air number for comparing the configurations is backed up. This affirms the assumption that only a part of the cooling air interacts with the reaction region.
The emission levels of unburned hydrocarbons (UHC), not shown in this section, are under the detection threshold for both combustors and all thermal powers apart from air numbers close to the LBO. Here, a rapid increase of UHCs is detectable due to incomplete combustion close to the blow-off limit.

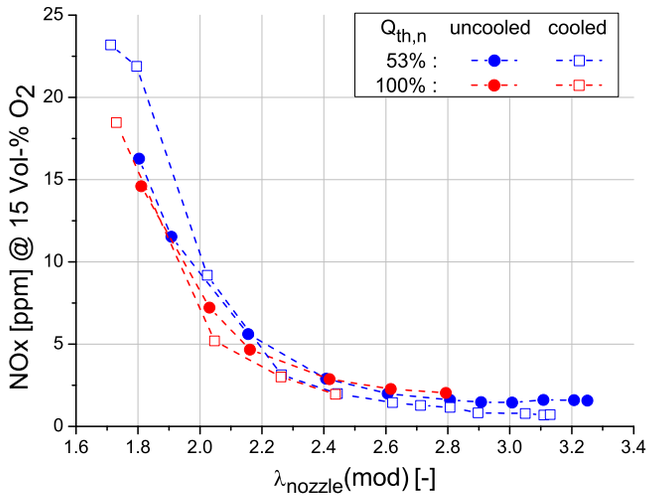

Figure 11. NOx Emissions of the Cooled and Uncooled Combustor Configurations as a Function of the Modified Air Number λ_{nozzle}(mod).

3.3. Flame shape and location

The flame characteristics regarding shape, location and homogeneity are discussed for both combustor designs in this section using time-averaged OH*-CL images. Figure 12 shows a series of OH*-CL images for the uncooled combustor configuration at $Q_{th,n}$ = 69% as a function of $\lambda_{overall}$. All images are scaled between zero and their maximum signal intensity. The corresponding scaling factors are indicated in the upper left corner. The points of origin of abscissa and ordinate mark the centre axis of the combustor and the combustor front plate, respectively. The dimensions are normalised with respect to the combustor diameter. Moreover, the azimuthal positions of the air nozzles located at the window in front of the camera are indicated at the bottom. Regarding the images at low overall air numbers discrete reaction zones around the entering fresh gas jets can be observed. Here, the reaction zones

http://dx.doi.org/10.5772/54405

are characterised by compact shape and distinctly separated flames. For air numbers between 2.2 and 2.4 the flame length stays approximately constant, whereas the height above burner (HAB) increases with rising $\lambda_{overall}$. Furthermore, for $2.2 \leq \lambda_{overall} \leq 2.8$ the reaction zones continuously merge into each other in horizontal direction evolving from separated flames to a single reaction region. For air numbers above 2.6 the reaction zone spreads in all spatial directions. Simultaneously, the HAB declines whereas the length of the reaction zone grows substantially. At $\lambda_{overall}$ = 3.1, which is the last operating point before LBO occured, the reaction zone is distributed over almost the whole combustion chamber volume. Moreover, regarding the scaling factors of the images the signal intensity decreases significantly with rising air numbers leading to a blueish visible flame of very low luminosity for $\lambda_{overall} \geq 2.8$.

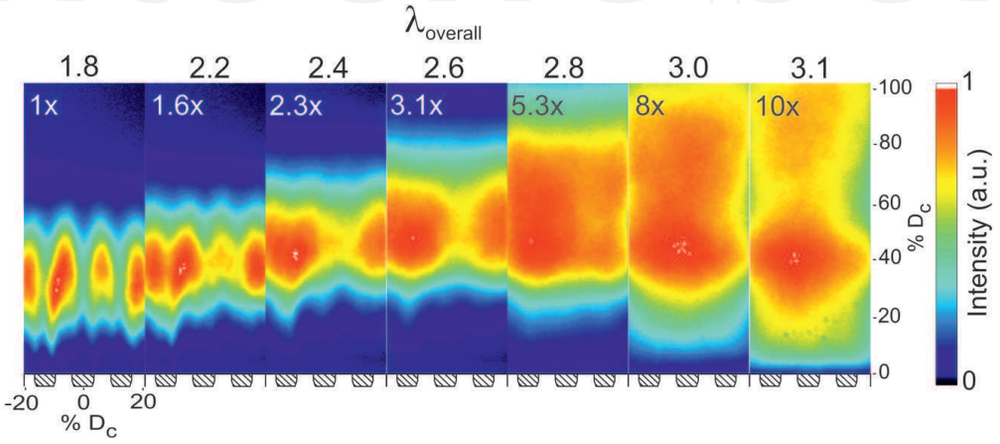

Figure 12. Time-averaged OH*-CL Images of the Uncooled Combustor at $Q_{th,n}$ = 69% as a Function of $\lambda_{overall}$.

In order to quantify and compare the phenomena observed in the time-averaged OH*-CL images, characteristic parameters are derived from the data. For the subsequent analysis only signals above 50% of the image maximum intensity are taken into account. This definition has been found as the most appropriate method to cover the image pixels corresponding visually to the flame. In the following these pixels are called reaction or flame region. With this definition the HAB equals the axial distance between the combustor front plate and the horizontally averaged lower flame boundary. The Dispersion of the OH*-signal is defined as the area of the flame region divided by the overall area of OH*-measurement. Therefore, the dispersion is a marker for the relative reaction volume, but not for its homogeneity. The horizontal distribution of the reaction regions is evaluated by the Relative Horizontal Inhomogeneity dI_{Flame}/dx. This parameter is calculated by vertically averaging the horizontal spatial intensity gradients inside the reaction regions and normalising it to the flame average intensity of each image. This definition ensures that dI_{Flame}/dx is comparable for different signal intensity levels and flame shapes. The Relative Horizontal Inhomogeneity is a marker for the discreetness of the flames in horizontal direction declining for merging reaction regions.

Figure 13 visualises the Dispersion of OH*-signal of the uncooled combustor design for all thermal powers as a function of $\lambda_{overall}$. Regarding $Q_{th,n}$ = 100% the dispersion stays approximately constant at 25% between $\lambda_{overall}$ = 1.8 and 2.15. For $\lambda_{overall} \geq 2.4$ the magnitude increases significantly up to 73%. This means that with rising Dispersion of OH*-signal the occupied volume of the reaction region inside the combustion chamber increases substantially until the flame is distributed over almost the whole volume. This

indicates a decrease of the Damköhler number which means that the chemical time scale increases in relation to the fluid dynamic time scale [21, 22]. An important influence factor for this behaviour is the exhaust gas recirculation rate which is enhanced by higher jet velocities and higher air numbers [11], respectively. Increasing recirculation serves to enhance the dilution of the fresh gas jets by hot flue gases [23] reducing the chemical reaction rates [24]. Simultaneously, rising jet velocity decreases the fluid dynamic time scale. Thus, both effects lead to a declining Damköhler number. On the other hand by increasing the air number the premixing quality of the air/fuel jets is altered as well. Since these quantities cannot be separated in the recent study, the major influence factor cannot be determined.
The general trend of the Dispersion of OH*-signal of the uncooled combustor design is similar for all thermal powers. However, the magnitude of the region of constant dispersion at low air numbers decreases for declining power from 25% at $Q_{th,n}$ = 100% down to 14% at $Q_{th,n}$ = 35%. The point of ascending dispersion is located between $\lambda_{overall}$ = 2.4 and 2.6 for all thermal powers but no distinct shift of this point can be observed for the uncooled configuration. In terms of reducing temperature peaks and simultaneously reducing NOx emissions, the rapid rise of the Dispersion of OH*-signal is desireable. However, for the application inside a MGT combustion system the available combustion chamber length limits the feasible volumetric expansion of the reaction region as discussed in section 1. At LBO-near conditions the flame region is expanded substantially so that the reaction process even continue after leaving the exhaust gas duct of the atmospheric test rig. Since operating pressure as well as wall heat loss also have a distinct effect on the flame characteristics, a final selection of the maximum feasible operating point can only be made on the base of a measurement campaign in the MGT test rig.

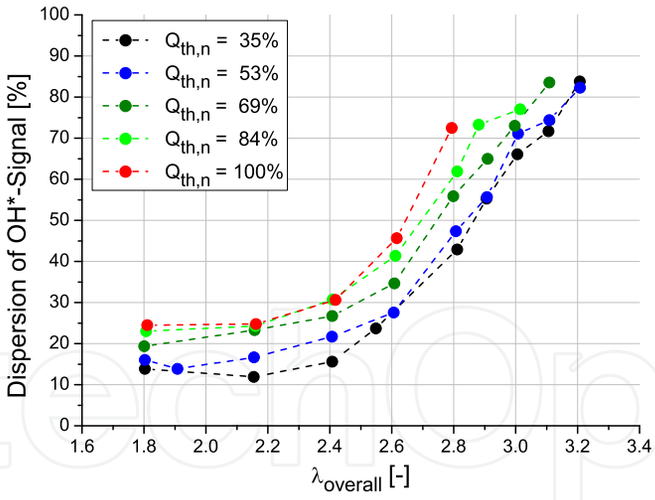

Figure 13. Dispersion of OH*-signal for the Uncooled Combustor Configuration.

Figure 14 presents the Dispersion of OH*-signal of the cooled combustor configuration for all thermal powers as a function of $\lambda_{overall}$. In contrast to the uncooled design, shown in figure 13, the cooled configuration exhibits with a range between 15% and 20% a similar magnitude of the region of constant dispersion at low air numbers for all thermal powers. Moreover, the point of ascending dispersion shifts with decreasing thermal power towards higher overall air numbers. This means that for a constant $\lambda_{overall} \geq 2.6$ higher thermal powers show a higher dispersion of the OH*-signal occupying a significantly larger combustion chamber volume.

http://dx.doi.org/10.5772/54405

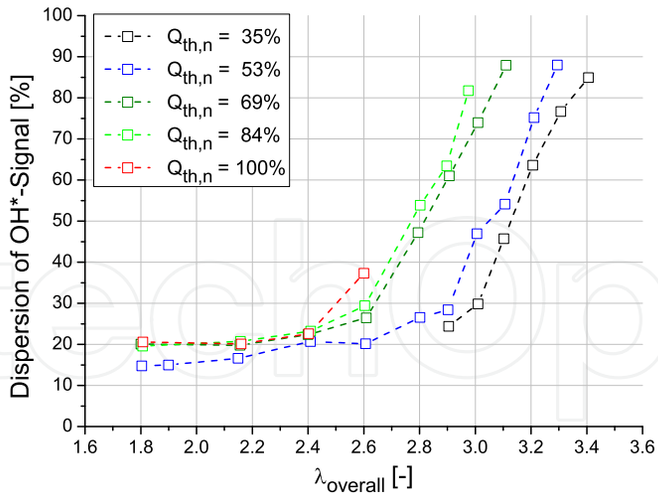

Figure 14. Dispersion of OH*-signal for the Cooled Combustor Configuration.

The height above burner of the cooled combustor design is visualised in figure 15 for all thermal powers as a function of $\lambda_{overall}$. This quantity describes the axial distance between the lower flame boundary and the combustor front plate. In the following graphs the HAB is presented normalised with respect to the combustor radius. Regarding the profile at $Q_{th,n}$ = 69% the HAB rises from 42% at $\lambda_{overall}$ = 1.8 up to 68% at $\lambda_{overall}$ = 2.6. At this air number the flame reaches its maximum lift-off height for $Q_{th,n}$ = 69%. With increasing air numbers beyond this point the HAB declines significantly exhibiting at LBO-near conditions with 23% its lowest magnitude. All HAB profiles at different thermal powers show a similar trend as well as a similar maximum lift-off height. However, for decreasing thermal power the profiles are shifted to higher overall air numbers exhibiting lower magnitudes at low air numbers. As described above, the recirculation rate intensifies at rising thermal power. Owing to higher jet velocities and enhanced fresh gas dilution by recirculated flue gases, the lift-off height increases with rising thermal power at low overall air numbers. Furthermore, the maxima of the HAB profiles are directly related to the points of ascending Dispersion of OH*-signal in figure 14. Due to the shift from discrete reaction zones into a volumetric combustion the reaction region expands to all spatial directions explaining the descent of the HAB. For high $\lambda_{overall}$ this effect of expanding reaction regions outbalances the increase of lift-off height caused by higher jet velocities at rising thermal powers which dominates at low air numbers.

The HAB profiles of both combustor designs are visualised in figure 16 as a function of λ_{nozzle}(mod) for $Q_{th,n}$ = 53% and 100%. The graph shows that the profiles of the presented thermal powers fit very well for both combustor configurations. It should be mentioned that this behaviour is consistent with all measured thermal powers. This behaviour demonstrates that the HAB is not affected by the cooling air when both combustors are compared as a function of λ_{nozzle}(mod). However, λ_{nozzle}(mod) is based on a shift of λ_{nozzle} to higher air numbers for the cooled combustor configuration. Therefore, identical profiles of the cooled and uncooled designs illustrate that the cooling air shifts the flame properties to lower nozzle air numbers compared to the uncooled design. In addition, this indicates that the chosen definition of the modified nozzle air number λ_{nozzle}(mod), which is based on the shift of the CO profiles, is in good agreement with the flame characteristics as well. This affirms the assumption that only a part of the cooling air participates in the reaction process.

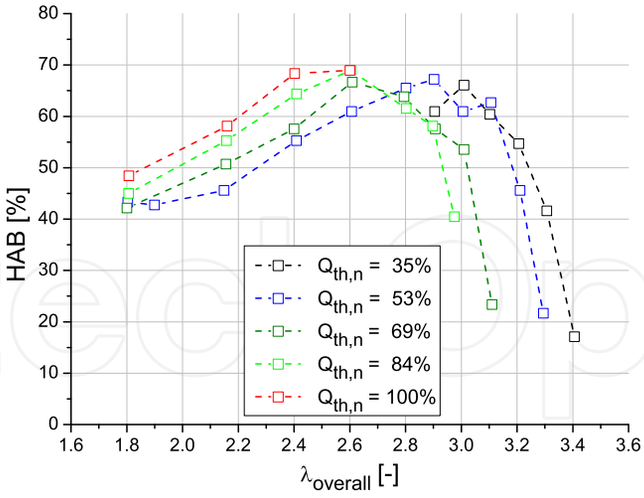

Figure 15. HAB for the Cooled Combustor Configuration as a Function of $\lambda_{overall}$.

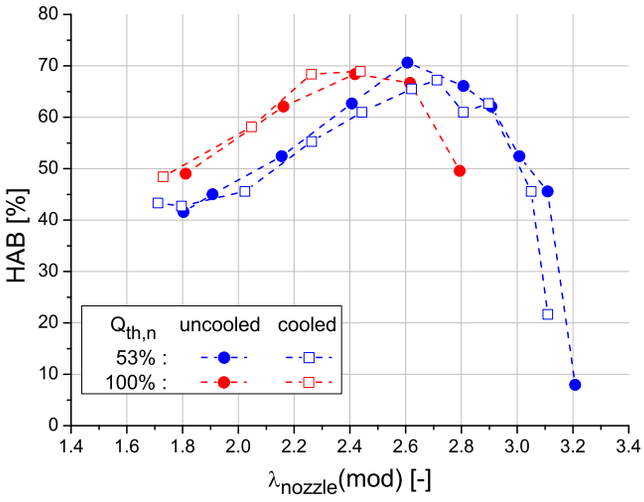

Figure 16. HAB for the Cooled and Uncooled Combustor Designs as a Function of λ_{nozzle}(mod).

Figure 17 visualises the Relative Horizontal Inhomogeneity dI_{Flame}/dx for the uncooled combustor configuration for all thermal powers as a function of $\lambda_{overall}$. This quantity describes the discreetness of the reaction zones in horizontal direction. The profile at $Q_{th,n}$ = 100% exhibits an inhomogeneity of 1.4 %/dPixel at $\lambda_{overall}$ = 1.8 converging exponentially with increasing air numbers towards a lower threshold of approximately 0.5 %/dPixel which is reached at $\lambda_{overall} \geq 2.6$. This means that for lower air numbers separated flames around the penetrating fresh gas jets exist, which merge together for rising air numbers resulting in a horizontally distributed reaction region for high $\lambda_{overall}$. The profiles of all thermal powers exhibit a lower threshold of the same magnitude which is reached at LBO-near conditions. The general trend of the profiles is similar for $53\% \leq Q_{th,n} \leq 100\%$. Only the profile at $Q_{th,n}$ = 35% differs from the exponential declining trend. However, at low overall air numbers the profiles' magnitudes are staggered in thermal power reaching higher values for low $Q_{th,n}$. This signifies that higher thermal powers exhibit better horizontally distributed flames which is due to an enhanced recirculation rate, better premixing quality at high flow rates as well as an enhanced interjet mixing rate.

http://dx.doi.org/10.5772/54405

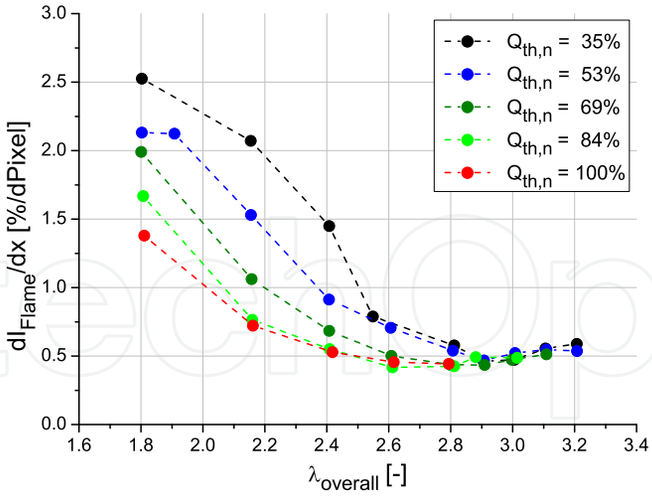

Figure 17. Relative Horizontal Inhomogeneity for the Uncooled Combustor Design as a Function of $\lambda_{overall}$.

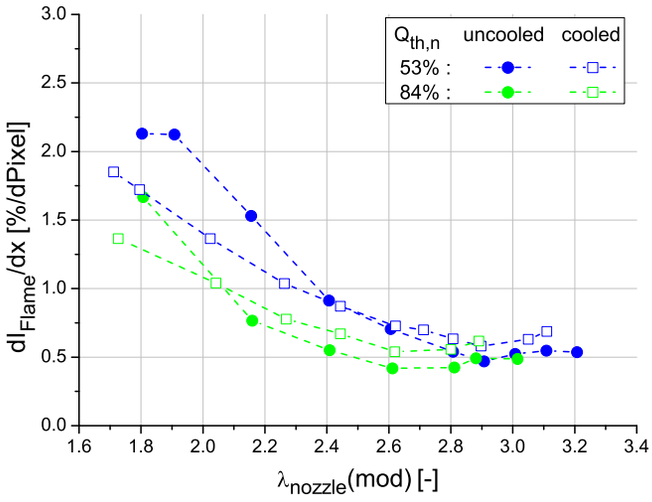

Figure 18. Relative Horizontal Inhomogeneity for the Cooled and Uncooled Combustor Designs as a Function of λ_{nozzle}(mod).

The comparison of dI_{Flame}/dx between the uncooled and the cooled combustor configuration is presented in figure 18 as a function of λ_{nozzle}(mod) for $Q_{th,n}$ = 53% and 84%. These thermal powers are chosen exemplarily since the occuring effects are well pronounced for these profiles but it should be mentioned that the discussed behaviour applies to all thermal powers. For rising λ_{nozzle}(mod) the curves of both designs show a similar declining trend of dI_{Flame}/dx at all $Q_{th,n}$. For higher air numbers the profiles of the cooled and uncooled configurations fit very well in magnitude at a constant thermal power converging to a similar lower threshold of approximately 0.5 %/dPixel. However, at low air numbers the uncooled design distinctly exhibits higher magnitudes of the Relative Horizontal Inhomogeneity. The difference of both designs decreases with rising thermal power as well as rising air number. This means that the difference in dI_{Flame}/dx decreases with increasing axial jet velocity u_{nozzle}. As shown in figure 2 the cooling air penetrates the combustion chamber through small exit holes located between the air nozzles. Since the split between cooling air and process air is almost constant over the whole operating range, the cooling jet velocity scales with the axial jet velocity u_{nozzle} and air number, respectively. Figure 18 indicates that for

lower jet velocities the penetrating cooling air serves to broaden the discreet reaction regions horizontally and therefore to homogenise their distribution. However, the homogenising of the flame regions for the cooled combustor configuration seems to have no effect on exhaust gas emissions at low air numbers as shown in figure 10 and 11.

4. Conclusion

A FLOX©-based micro gas turbine combustor was introduced. The presented experimental study compared an impingement cooled combustor configuration to an uncooled design for natural gas. The influence of selected operating conditions on shape, location and homogeneity of the reaction zones was analysed under atmospheric conditions using time-averaged OH*-chemiluminescence images. Furthermore, the dependencies of jet velocity and combustor front plate cooling on LBO limits were discussed. Exhaust gas emissions were presented and a definition of a modified nozzle air number was derived from comparing the CO profiles of the cooled and uncooled design. With the help of this parameter the differences of both designs were analysed.
Regarding the parameters derived from OH*-chemiluminescence images a distinct increase of Dispersion of OH*-signal was observed for rising air numbers leading to a volumetric reaction region at LBO-near conditions. Simultaneously, the detachedness and the horizontal inhomogeneity of the reaction regions reduced substantially. The influence of the cooling air was observed to generate a shift of all emission and flame profiles to lower nozzle air numbers. However, it was discussed that only a part of the cooling air interacts with the reaction region whereas the rest of the cooling air passes the combustion chamber without participating in the combustion process. Moreover, it was shown that with the cooled combustor design higher overall air numbers can be realised at low thermal powers which is advantageous if the amount of combustion air is to be maximised.

Acknowledgements

The financial support of this work by the EnBW Energie Baden-Württemberg AG and the German Federal Ministry of Economics and Technology is gratefully acknowledged. Furthermore, the authors would like to thank Marco Graf for his support.

Author details

Zanger Jan*, Monz Thomas and Aigner Manfred

* Address all correspondence to: jan.zanger@dlr.de

German Aerospace Center, Institute of Combustion Technology, Stuttgart, Germany

References

[1] Bhatt M S (2001) Mapping of General Combined Heat and Power Systems, Energy Conversion and Management 42, pp. 115-4.

[2] Pilavachi P A (2000) Power Generation with Gas Turbine Systems and Combined Heat and Power, Applied Thermal Engineering 20, pp. 1421-1429.

http://dx.doi.org/10.5772/54405

[3] Fritsche D, Füri M, Boulouchos K (2007) An Experimental Investigation of Thermoacoustic Instabilities in a Premixed Swirl-stabilized Flame, Combustion and Flame 151, pp. 29-36.

[4] Huang Y, Yang V (2009) Dynamics and Stability of Lean-premixed Swirl-stabilized Combustion, Progress in Energy and Combustion Science 35, pp. 293-364.

[5] Nauert A, Peterson P, Linne M, Dreizler A (2007) Experimental Analysis of Flashback in Lean Premixed Swirling Flames: Conditions Close to Flashback, Exp Fluids 43, pp. 89-100.

[6] Wünning, J.A. and Wünning, J.G.(1997) Flameless Oxidation to Reduce Thermal NO-Formation, Prog. Energy ComlnaL Sci.23, pp. 81-94.

[7] Hamdi M, Benticha H, Sassi M (2012) Fundamentals and Simulation of MILD Combustion, Thermal Power Plants, Dr. Mohammad Rasul (Ed.), ISBN: 978-953-307-952-3, InTech. pp. 43-64.

[8] Weber R, Smarta J P, vd Kamp W (2005) On the (MILD) Combustion of Gaseous, Liquid and Solid Fuels in High Temperature Preheated Air, Proceedings of the Combustion Institute, Vol. 30, pp. 2623-2629

[9] Arghode V K, Gupta A K (2010) Effect of Flow Field for Colorless Distributed Combustion (CDC) for Gas Turbine Combustion, Applied Energy 87(5), pp. 1631-1640.

[10] Tsuji H, Gupta A K, Hasegawa T, Katsuki M, Kishimoto K, Morita M (2003) High Temperature Air Combustion, CRC Press, Florida.

[11] Li G, Gutmark E J, Stankovic D, Overman N, Cornwell M, Fuchs L, Vladimir M (2006) Experimental Study of Flameless Combustion in Gas Turbine Combustors, Proceedings of 44th AIAA Aerospace Sciences Meeting and Exhibit, AIAA 2006-546.

[12] Lückerath R, Meier W, Aigner M (2007) FLOX© Combustion at High Pressure with Different Fuel Compositions, Proceedings of GT2007 ASME Turbo Expo 2007, GT2007-27337.

[13] Lammel O, Schütz H, Schmitz G, Lückerath R, Stöhr M, Noll B, Aigner M (2010) FLOX© Combustion at High Power Density and High Flame Temperatures, Proceedings of GT2010 ASME Turbo Expo 2010, GT2010-23385.

[14] Schütz H, Lückerath R, Kretschmer T, Noll B, Aigner M (2006) Analysis of the Pollutant Formation in the FLOX© Combustion, Proceedings of GT2006 ASME Turbo Expo 2006, GT2006-91041.

[15] Duwig C, Stankovic D, Fuchs L, Li G, Gutmark E (2008) Experimental and Numerical Study of Flameless Combustion in a Model Gas Turbine Combustor, Combustion Science and Technology 180, pp. 279-295.

[16] Lammel O, Stöhr M, Kutne P, Dem C, Meier W, Aigner M (2011) Experimental Analysis of Confined Jet Flames by Laser Measurement Techniques, Proceedings of GT2011 ASME Turbo Expo 2011, GT2011-45111.

[17] Dandy D S, Vosen S R (1992) Numerical and Experimental Studies of Hydroxyl Radical Chemiluminescence in Methane-Air Flames, Combustion Science and Technology 82, pp. 131-150.

[18] Vaz D C, Buiktenen J P, Borges A R J, Spliethoff H (2004) On the Stability Range of a Cylindrical Combustor for Operation in the FLOX Regime, Proceedings of GT2004 ASME Turbo Expo 2004, GT2004-53790.

[19] Lefevbre A H, Ballal D R (2010) Gas Turbine Combustion: Alternative Fuels and Emissions – 3rd ed., CRC Press, Boca Raton.

[20] Joos F (2006) Technische Verbrennung, Springer, Berlin.

[21] Borghi R (1985) On the Structure and Morphology of Turbulent Premixed Flames, Recent Advances in Aerospace Sciences, Plenum Press, New Yorck.

[22] Sadanandan R, Lückerath R, Meier W, Wahl C (2011) Flame Characteristics and Emissions in Flameless Combustion Under Gas Turbine Relevant Conditions, Journal of Propulsion and Power 27(5), pp. 970-980.

[23] Levy Y, Rao G A, Sherbaum V (2007) Preliminary Analysis of a New Methodology for Flameless Combustion in Gas Turbine Combustors, Proceedings of GT2007 ASME Turbo Expo 2007, GT2007-27766.

[24] Li P, Mi J, Dally B B, Wang F, Wang L, Liu Z, Chen S, Zheng C (2010) Progress and recent trend in MILD combustion, Science China Technological Sciences 54(2), pp. 255-269.